Ti-Modified Imogolite Nanotubes as Promising Photocatalyst 1D Nanostructures for H 2 Production

Pablo Jimenéz-Calvo, Yassine Naciri, Anna Sobolewska, Mark Isaacs, Yu Zhang, Amélie Leforestier, Jéril Degrouard, Stéphan Rouzière, Claire Goldmann, Delphine Vantelon, et al.

Ti-Modified Imogolite Nanotubes as Promising Photocatalyst 1D Nanostructures for H_2 Production

Pablo Jimenéz-Calvo,[*†] *Yassine Naciri,*[†] *Anna Sobolewska, Mark Isaacs, Yu Zhang, Amélie Leforestier, Jéril Degrouard, Stéphan Rouzière, Claire Goldmann, Delphine Vantelon, Simon Hettler, Nestor J. Zaluzec, Raul Arenal, Pascale Launois, Mohamed Nawfal Ghazzal*[*] *and Erwan Paineau*[*]

P. Jimenéz-Calvo, Y. Naciri, A. Sobolewska, A. Leforestier, J. Degrouard, S. Rouzière, C. Goldmann, P. Launois, E. Paineau
Université Paris-Saclay, CNRS, Laboratoire de Physique des Solides, 91405 Orsay, France
E-mail: erwan-nicolas.paineau@universite-paris-saclay.fr

P. Jimenéz-Calvo
Present address: Friedrich-Alexander Universität Erlangen-Nürnberg, Department for Materials Sciences, Martensstrasse 7 and Chemistry of Thin Film Materials, IZNF, Cauerstraße 3, D-91058 Erlangen, Germany. E-Mail: pablo.jimenez.calvo@fau.de

Y. Naciri, A. Sobolewska, M. N. Ghazzal
Université Paris-Saclay, UMR 8000, CNRS, Institut de Chimie Physique, 91405 Orsay, France. E-mail: mohamed-nawfal.ghazzal@universite-saclay.fr

M. Isaacs
HarwellXPS, Research Complex at Harwell, Rutherford Appleton Laboratories, Didcot OX11 0FA, UK. University College London, Department of Chemistry, 20 Gordon Street, London, WC1H 0AJ, UK

Y. Zhang
Central Laser Facility, STFC Rutherford Appleton Laboratory, Didcot 0X11 0QX, UK

D. Vantelon
Synchrotron SOLEIL, L'Orme des Merisiers, 91192 Gif-sur-Yvette Cedex, France

S. Hettler, R. Arenal
Instituto de Nanociencia y Materiales de Aragon (INMA), CSIC-Universidad de Zaragoza, Spain. Laboratorio de Microscopias Avanzadas (LMA), Universidad de Zaragoza, E-50018 Zaragoza, Spain.

R. Arenal

Araid Foundation, E-50018 Zaragoza, Spain

N. J. Zaluzec

Argonne National Laboratory / Photon Science Directorate, Lemont, Illinois, USA

† These authors contributed equally

Keywords: nanotube, polarization, photocatalysis, hydrogen, multi-scale analysis

Abstract. Imogolite nanotubes are predicted as a unique one-dimensional material with spatial separation of conduction and valence bands edges but their large band gaps have inhibited their use as photocatalysts. The first step toward using these nanotubes in photocatalysis and exploiting the polarization-promoted charge separation across their walls is to reduce their band gap. Here, we explore the modification of double walled aluminogermanate imogolite nanotubes by incorporation of titanium into the nanotube walls. The precursor ratio x = [Ti]/([Ge]+[Ti]) is modulated between 0 to 1. Structural and optical properties are determined at different scales and the photocatalytic performance is evaluated for H_2 production. Although the incorporation of Ti atoms into the structure remains limited, the optimal condition is found around x = 0.4 for which the resulting nanotubes reveal a remarkable hydrogen production of ~1500 µmol g^{-1} after 5h for a noble metal-free photocatalyst, a 65-fold increase relative to a commercial TiO_2-P25. This is correlated to a lowering of the recombination rate of photogenerated charge carrier for the most active structures. These results confirm the theoretical predictions regarding the potential of modified imogolite nanotubes as photoactive nanoreactors and pave the way for investigating and exploiting their polarization properties for energy applications.

1. Introduction

One-dimensional nanostructures such as nanotubes (NTs) have attracted attention in sunlight-driven photocatalytic applications owing to their competitive advantages compared to bulk materials.[1–3] 1D nanostructures exhibit intrinsic structural features offering potential solutions to current challenges facing photocatalytic materials, namely charge carrier recombination, low specific surface area, and light-harvesting properties.[4] They have shown fast and long-distance electron transport, a high yield of charge carrier separation, a high reactive surface area, and improved absorbance properties. Owing to these properties, a wide range of 1D-based nanostructure materials have been developed for photocatalytic application.[5–9] These nanostructures provide higher photoactivity but the coupling with

metallic nanoparticles or semiconductors with adequate potential energies is required to extend the lifetime of the photogenerated charge carriers.[10–13] A promising strategy has emerged recently by exploiting the surface charge separation promoted by the electric field caused by an intrinsic dipole moment in the nanostructure.[14] This electric field induces the splitting of excitonic pairs in spatially-separated sites within the photocatalytic material, thus allowing control of the overall drive and kinetics of redox reactions.

In this context, imogolite nanotubes (INTs) with chemical formula $(Si,Ge)Al_2(OH)_3O_3R$ (where R = OH, CH_3…), appear as alternative materials of well-defined morphology (single or double-walled) with tunable monodisperse diameters and scalable inner/outer interfaces (e.g. hydrophilic or hydrophobic surfaces).[15–17] Recently, density functional theory (DFT) studies suggested that INTs could be the ideal photocatalyst, offering at the same time high reactive surface area and natural charge carrier separation thanks to its permanent polarization.[18–20] The originality of these nanotubes stems from the atypical spatial separation of the valence (VB) and conduction band (CB) edges across the nanotube walls; promoting redox reactions at separated locations.[18,19] This unique VB/CB configuration could result in enhanced photocatalytic efficiency.[21–23] However, the use of such behavior is inhibited by the high electrostatic band gap of imogolite nanotubes, estimated in the range 3-7 eV, based on tight-binding [24,25] or generalized gradient approximations[18,19] DFT methods, which tend to over or underestimate the band gap, respectively. The wide band gap[24,25] and the band edge energies positions of CB and VB make difficult to perform the proton reduction spontaneously with imogolite nanotubes without any modification of the structure. A promising step is the doping of the nanotube lattice by various metal cations but has been rarely explored. From an experimental point of view, only Fe-doped imogolite nanotubes have been obtained so far, with applications restricted to photoFenton degradation of dyes.[26,27] However, DFT calculations evidenced that doped imogolite-like structures should display a decrease in band gap with the incorporation of different transition metals or rare-earth elements.[28,29] In this framework, we explore the potential of aluminogermanate double-walled INTs (DWINTs) as suitable photocatalysts since the permanent dipole density at the walls results in an electro-negative inner tube while the outer tube displays an electropositive surface.[18] To enhance their optical properties, we dope the nanotube structure with Ti atoms (**Figure 1**) while preserving the DW shape, allowing to provide promising photoactive imogolite nanotubes for H_2 generation.

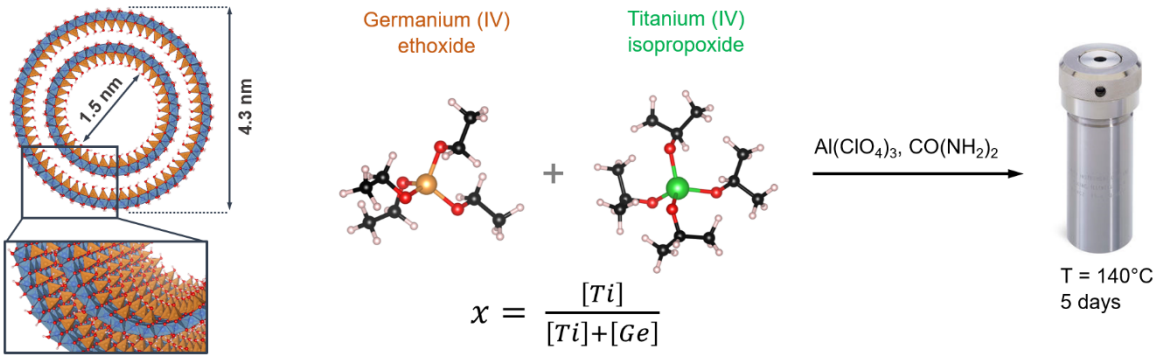

Figure 1. (left) Schematic view of a DWINT structure with Al, Ge and O atoms represented in blue, orange and red, respectively. (right) Proposed method to dope imogolite nanotubes with Ti atoms at different precursor ratio *x*.

2. Results and Discussion

DWINTs doped with Ti are synthesized by adapting the method proposed by Amara et al.[30] The precursors ratio defined as *x* = [Ti]/([Ge]+[Ti]) is modulated in the range of x = 0 to 1 (see Experimental section). We first characterized the obtained samples depending on the initial precursor ratio. Morphological investigations by conventional transmission electron microscopy (TEM) reveal the preservation of the nanotube shape up to x = 0.4 (**Figure S1**), though at the expense of length that is shortened with Ti-doping (**Figure S2** and **Table S1**). For a higher precursor ratio (x ≥ 0.6), ellipsoid plate-like particles and dense spherical aggregates are dominant (**Figure S1**) corresponding respectively to AlO(OH) boehmite[31] and TiO_2 anatase nanoparticles[32], as demonstrated later. High-resolution cryo-TEM observations (**Figure 2a**) on pristine (x = 0) Ge sample and Ti/Ge samples (x = 0.2 and 0.4) confirm unambiguously the formation of double-walled nanotubes with monodisperse inner (~1.5 nm) and outer (~4.3 nm) diameters (**Figure S3** and **Table S1**). Closer observation also reveals that nanotubes synthesized with Ti may have some structural defects within the walls or occasionally form nanoscrolls (**Figure S4**). These findings point to the fact that there is a limit to the incorporation of Ti beyond which the tubular structure can no longer be formed.

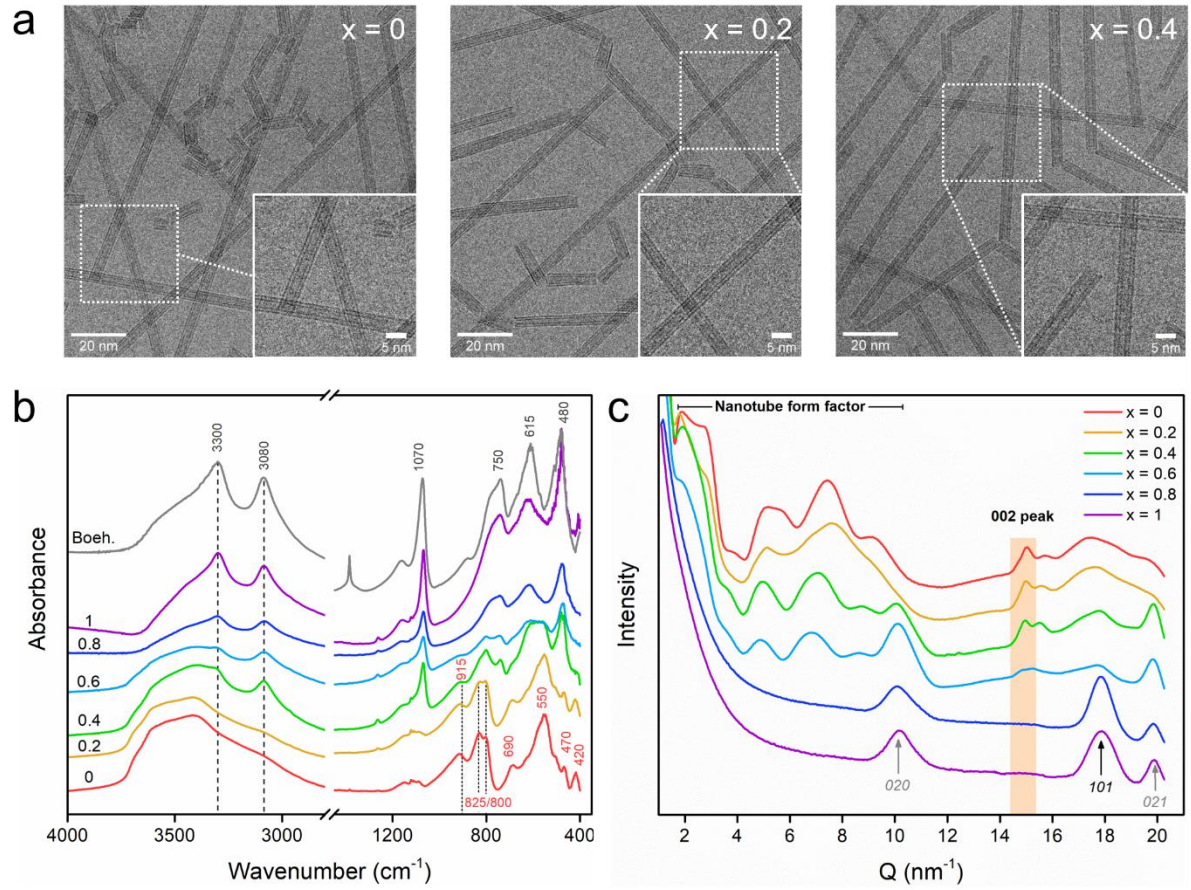

Figure 2. (a) cryo-TEM images of Ti/Ge samples synthesized at different doping ratios *x* = 0, 0.2 and 0.4. The insets in panel c are higher magnification images of the tubular structure. Characterization of the different Ti/Ge samples synthesized with varying precursor ratio x. (b) FTIR spectra. The grey curve corresponds to a pure boehmite phase. (c) WAXS patterns. Grey and black arrows, respectively, show an indexation of boehmite and anatase reflections. In b and c, the curves have been translated vertically for the sake of clarity.

The structural characteristics of the different Ti/Ge samples are assessed by combining Fourier-transform infrared (FTIR) spectroscopy and wide-angle X-ray scattering (WAXS) experiments. FTIR spectra of the Ti/Ge samples prepared at *x* = 0.2 and 0.4 are similar to the reference Ge-DWINT sample (*x* = 0) (**Figure 2b**). The absorption bands at 915 cm^{-1} and the doublet at 825 and 800 cm^{-1} correspond to Ge-O stretching vibrations in the tubular structure of the INT.[33,34] The IR bands at 690 and 550 cm^{-1} are ascribed to Al-O stretching modes, while the signals at 470 and 420 cm^{-1} are related to –OH, Ge-O-Al, and O-Ge-O bending modes for aluminogermanate imogolite nanotubes.[34,35] All samples also present a large absorption band in the OH stretching region with two main signals at 3450 and 3100 cm^{-1} corresponding to external and internal OH groups attached to (OH)Al and (OH)Ge,

respectively.[36] Above a 0.4 doping ratio, the INT signature is progressively lost, and new well-resolved absorption peaks occur at 3300, 3080, 1070, 750, 615, and 480 cm^{-1} attributed to the boehmite structure.[37] The stretching modes of Ti-O-Ti (around 690 cm^{-1}) are probably present but overlap with the FTIR signal from boehmite. WAXS experiments also highlight the effect of precursor ratio on the structure of imogolite nanotubes. Scattering intensity profiles reveal broad modulations (**Figure 2c** and **Figure S5**). At a low doping ratio ($x \leq 0.4$), the scattered intensity below 10 nm^{-1} mainly displays oscillations characteristic of the form factor of DW nanotubes,[38–40] showing that the nanotubes are not aggregated in large bundles. This DW signature is still present for the sample (x = 0.6). Interestingly, the axial periodicity along the nanotube axis (which results in the asymmetrical peak[20] located around 15 nm^{-1}) remains unchanged with increasing the doping ratio up to 0.6. No nanotube signal is observed for x = 0.8 and 0.1. Boehmite and anatase phases are observable for $x \geq 0.4$ (**Figure S5**). Understanding the local structural modifications of the nanotubes is essential for further investigation of the photoinduced properties of these doped-nanostructures. We performed X-ray photoelectron spectroscopy to investigate the chemical composition and oxidation states of elements at the INTs surface. The survey spectrum of INTs shows the main contributions of Ge 2p, O 1s, and Al 2p (**Figure S6**).

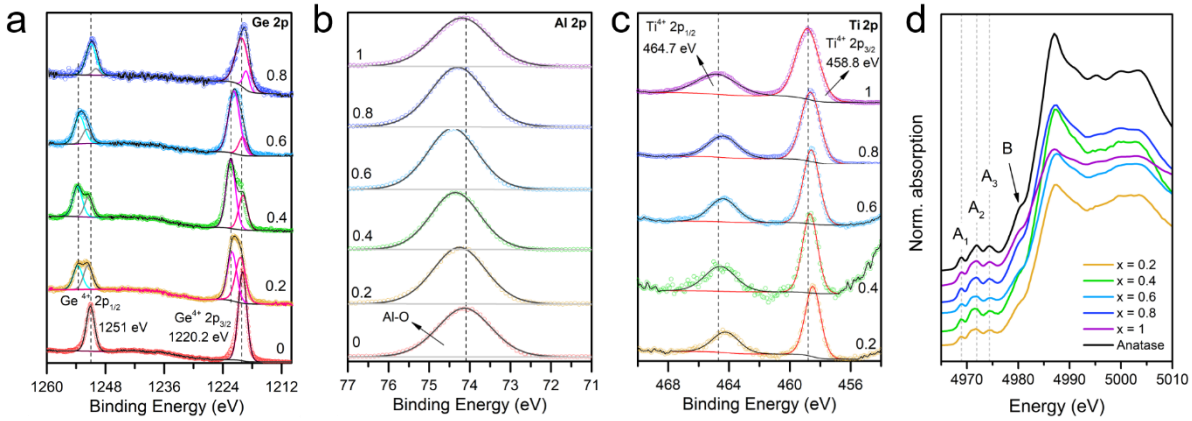

Figure 3. XPS spectra for (a) Ge 2p, (b) Al 2p and (c) Ti 2p. (d) XANES spectra at the Ti K-edge. In all panels, the curves have been translated vertically for the sake of clarity.

As expected, pure Ge-DWINT (x = 0) does not contain any Ti element. The peak at 1251 eV is assigned to Ge $2p_{1/2}$ whereas the one at 1220.2 eV to Ge $2p_{3/2}$ level of GeO (**Figure 3a**).[41–43] The Ti doping INTs with a ratio from 0 to 0.4 induces a noticeable enlargement of the Ge 2p peaks, which can be deconvoluted to two peaks. The new peak at higher energy (1222.4 eV) indicates the formation of Ge with a higher oxidation state as in GeO_2.[41,44] The Ge 3s

peak (**Figure S7a**) can be deconvoluted into two main peaks centered at 184.1 and 179.1 eV for w ≤ 0.6, which are attributed to Ge-O and Ge-O-Al bonds, respectively. By contrast, the Al 2p signal (**Figure 3b**) exhibits a single contribution at 74.1 eV, ascribed to Al-O bonding in octahedral sites.[45–47] We also notice a slight shift of the Al 2p signal towards higher binding energy with respect to the unmodified Ge-DWINT that could be related to a modification of the distortion in Al sites in boehmite compared to INTs at precursor ratio x > 0.4. The Ti-doping effect is investigated by recording the Ti 2p peak (**Figure 3c**). For x = 1, the spin–orbit components ($2p_{3/2}$ and $2p_{1/2}$) of the Ti 2p peak are well deconvoluted into two sharp peaks at 458.8 and 464.1 eV, respectively, characteristic of Ti^{4+} in TiO_2.[48] The measured separation between the Ti $2p_{3/2}$ and Ti $2p_{1/2}$ peaks is 5.7 eV, in agreement with the observed one for stoichiometric TiO_2.[49] Interestingly, these two components are shifted to lower binding energies (0.3 eV) as the ratio of Ti doping decreases, and the separation between the spin-orbit components is higher as well (5.98 eV), which points to a distortion of Ti sites. The O 1s signal (**Figure S7b**) exhibits two contributions around 533.0 and 531.9 eV, assigned to Al-O and Ge-O chemical bonds, respectively.[43,47,50] As the doping occurs, the O1s peak becomes larger and shifts toward lower binding energies. This is due to modification of the chemical environment provoked by the formation of O-Ti bond. The progressive evolution of XPS spectra with respect to the doping ratio suggests an incorporation of Ti atoms into the nanotube structure, probably in an octahedral configuration. To confirm the doping modification, we performed X-ray Absorption Near Edge Spectroscopy (XANES) at the Al K-edge (**Figure S8**). The first two samples (x = 0 and 0.2) present a large absorption band located at 1571 eV, characteristic of aluminum in an octahedral configuration.[51] With increasing [Ti]/([Ge]+[Ti]) precursor ratio, a lower energy resonance appears at 1567 eV related to the spectral feature of boehmite, which contains Al sites in a distorted octahedral configuration compared to imogolite nanotubes.[52] The amount of boehmite formed depends on the precursor ratio as demonstrated by linear combination fitting of XANES spectra using pure Ge-DWINT (x = 0) and the sample prepared at x = 1 that contains only boehmite as Al species (**Figure S8**). We also conducted XANES measurements at the Ti K-edge to determine the speciation of Ti atoms and the modification of the local environment for the different Ti/Ge samples (**Figure 3d**). The curves are quite similar to the one obtained for a reference anatase sample. XANES spectra present several pre-edge features before reaching the edge jump located around 4987 eV. The pre-edge region shows three well-resolved peaks (A_1-A_3), which are attributed to 1*s* to 3*d* dipolar transitions of Ti^{4+} in octahedral configuration as proposed by Farges et al.[53] The shoulder (B) around 4980 eV is

assigned to 1*s* to 4*p* transition of the TiO_6 octahedron in agreement with XPS analysis indicating the formation of stoichiometric TiO_2 in its anatase form. These results indicate that titanium incorporated into the walls of the nanotube seems to replace preferentially Al atoms. The large oscillations that follow the edge jump become better resolved and similar to those of anatase for doping levels above x = 0.6, in agreement with the increasing amount of anatase in the sample.

Finally, scanning transmission electron microscopy (STEM) analyses have been performed in order to further investigate the presence of titanium into the nanotube structure. **Figures 4a,b** show high-resolution high-angle annular dark field (HAADF) STEM images of nanotubes. Temporally-resolved hyperspectral X-ray energy dispersive spectroscopy (XEDS) has been performed in different nanotubes. The presence of sparse clusters of titanium at the nanotubes locations has been identified by the presence of minute Ti-K X-ray signals. An example of which can be observed in the XEDS spectrum displayed in **Figure 4c**. The distribution is rather heterogeneous throughout the nanotubes. In general, the amount of Ti within the nanotubes is extremely low, based upon our maximum observed Ti signal, we estimate that the Ti/Al ratio is < 0.01 when Ti is present. These structural observations prove the local doping of the imogolite structure with Ti atoms We note that titanium in the form of titanium oxide, has also been observed forming small nanoparticles for x = 0.4.

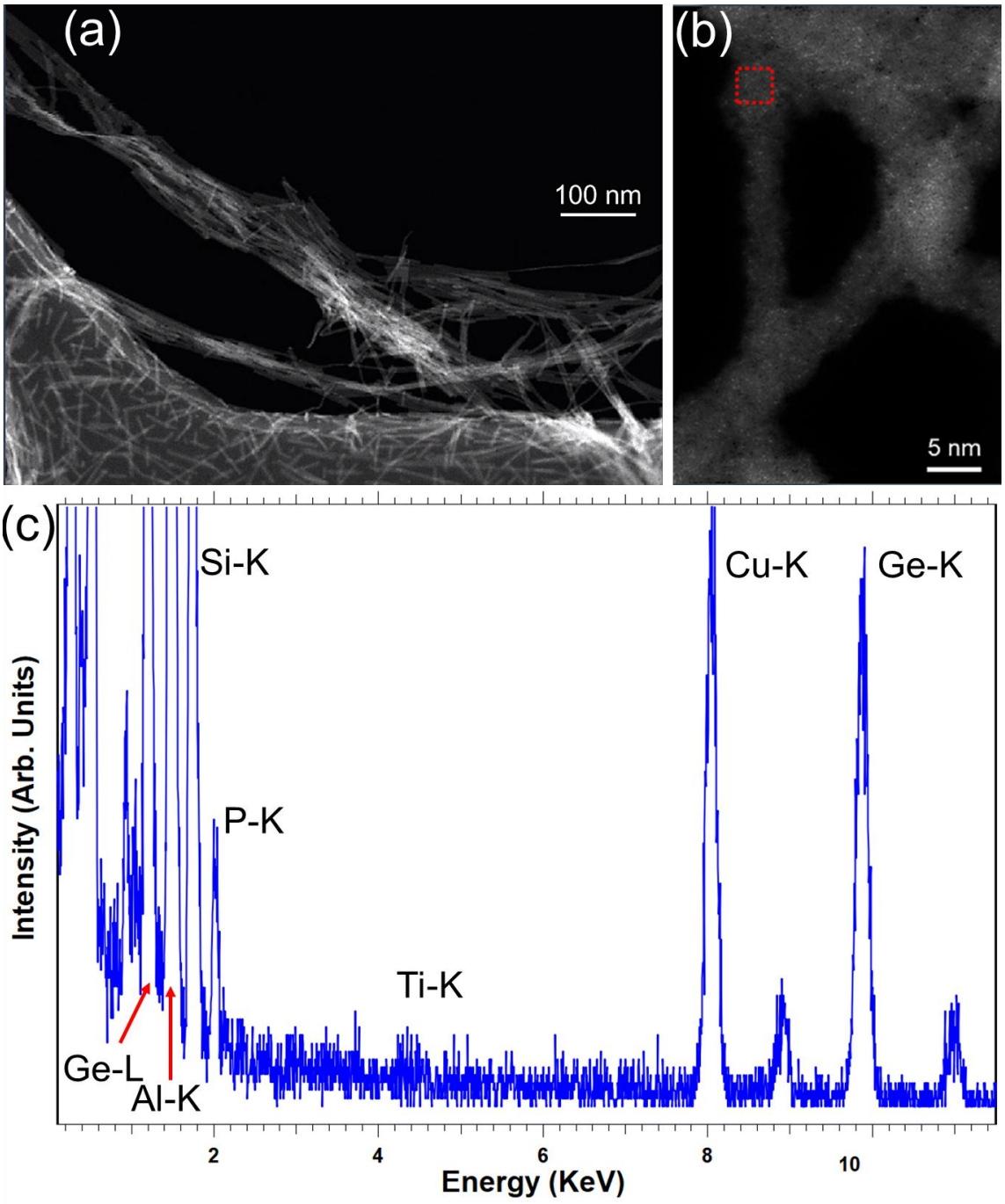

Figure 4. Scanning transmission electron microscopy (STEM) analyses of imogolite nanotubes. (a-b) High-angle annular dark field (HAADF)-STEM micrographs. (c) XEDS spectrum acquired from the red highlighted area in panel (b) on an individual nanotube. Titanium has been detected in this region of the nanotube as visible from the signal in the Ti-K X-ray emission.

After this structural characterization, the evolution of the optical properties is investigated using UV-vis spectroscopy (**Figure S9**). The samples exhibit an absorption band in the UV range (< 350 nm), typical of the creation of an optical band gap in semiconductors defined as

the difference between the valence band edge and conduction band edge. As the Ti ratio increases in the Ti/Ge samples, a redshift is observed, pointing to the doping effect on tuning of the optical band gap (**Figure S9**). From the Tauc plot analysis (**Figure 5a**), it can be ascertained that the band gap (E_g) energy drastically decreases from 4.35 eV (for pristine Ge-DWINT) to 3.96 eV (x = 0.2) and then to 3.92 eV (x = 0.4) (**Figure 5b**). Further increasing of the Ti/Ge ratio steadily decreases the E_g down to 3.85 eV. The latter band gap is similar to that obtained for anatase TiO_2,[49] in agreement with WAXS results. The valence band edge is determined from high-resolution XPS spectra at low binding energy (**Figure 5c**). Combined with the band gap energy obtained previously, we determine the conduction band edge of the different samples that are reported in the band energy alignment diagram in **Figure 5d**. The Ti-doping initially induces a downward shift of the VB edge (0.13 and 0.43 eV for 0.2 and 0.4 ratio, respectively), followed by an upward shift when the Ti/Ge ratio further increases. Similar behavior is observed for the CB edge, which shifts down to -0.13 eV (for 0.4 ratio), and up to -1.43 eV. Interestingly, this evolution with an optimum around x = 0.4 can be related to the disappearance of nanotubes in favor to boehmite and anatase phases as shown above. This band gap modification is expected to have a direct effect on the photocatalytic performance of the Ti/Ge samples.

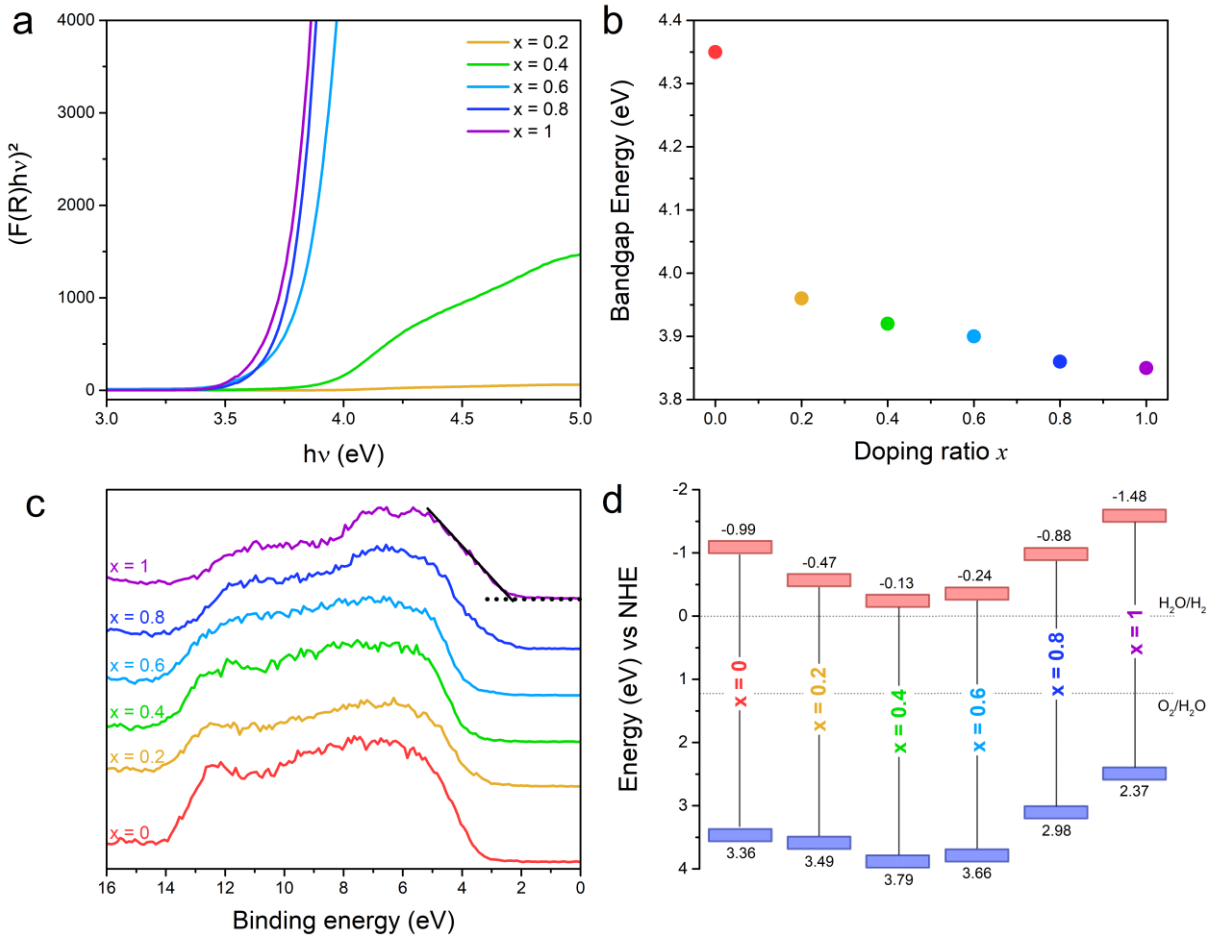

Figure 5. Optical and electronic properties of the Ti/Ge samples as a function of the substitution ratio: (a) Tauc plots; (b) evolution of the band gap energy E_g; (c) XPS spectra in the VB region and (d) corresponding energy diagram scheme.

In the following, we investigate the photocatalysis properties of Ti-doped imogolite nanotubes. The H_2 production activity is monitored over time under artificial solar-light irradiation (**Figure 6a**) to assess the Ti-doping effect on the photocatalytic efficiency of Ti/Ge samples up to x = 0.6 for which the nanotube structure is preserved, knowing that the latter already contains anatase nanoparticles. For comparative purposes, we also measure the H_2 production activity of TiO_2-P25 nanoparticles (Degussa) used here as a standard noble metal free photocatalyst as well as boehmite nanoparticles. As expected, Ge-DWINTs show negligible photoactivity for H_2 generation, which is due to the low absorbance properties at the energy excitation wavelength of the Xenon lamp as well as the large band gap of the sample. By contrast, Ti-doping samples for x = 0.2 and 0.4 exhibit 1509 and 1472 µmol g^{-1} of H_2 production, respectively, that is 65 times higher than the commercial TiO_2-P25 (23 µmol g^{-1}) under the same experimental condition.[54] The comparison with tubular TiO_2 photocatalysts is also instructive. Ge and al. provided a comprehensive review on hydrogen production by TiO_2 nanotubes with values ranging from 30 µmol.h^{-1}.g^{-1} up to 80 mmol.h^{-1}.g^{-1} but with the use of co-catalysts. Therefore, the 1500 µmol.h^{-1}.g^{-1} H_2 formation rate of our composite remaines as one of the highest H_2 generation for quasi-bare a, d TiO_2-based tubular materials without noble metals.[7] The Ti-doping downshifts the CB edges, reaching adequate potential for light absorption and efficient photogenerated charge separation that leads to an enhancement of H_2 generation efficiency. A further increase of the doping ratio impacts both the loss of the nanotube structure (the polarization effect) and the appearance of an inactive boehmite phase (**Figure 6a**), as evidenced previously, decreasing the photocatalytic activity. It underlines that the optimal ratio of Ti substitution is around 0.4.

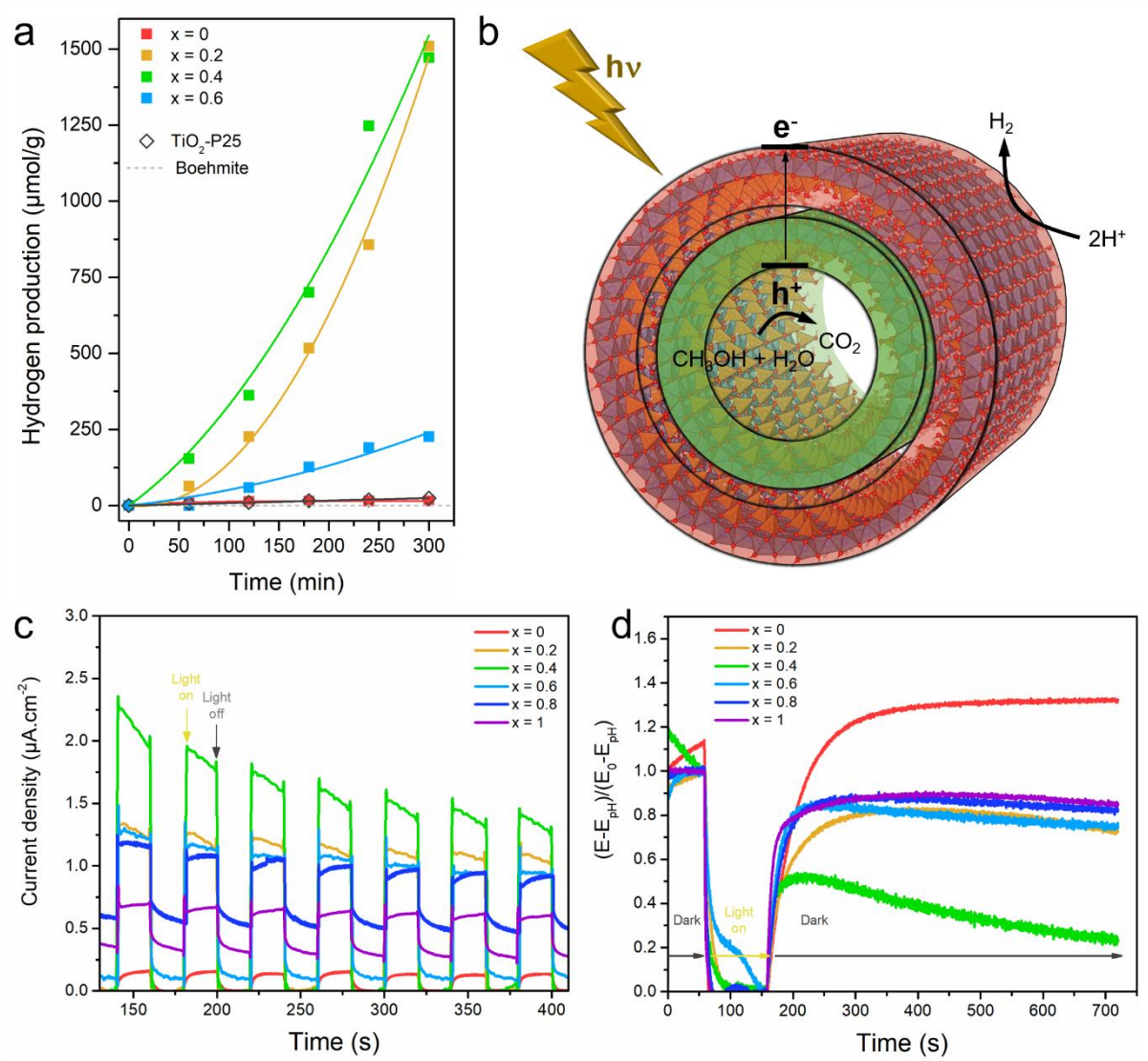

Figure 6. Hydrogen evolution reaction under solar-light irradiation for (a) Ge-DWINT and Ti/Ge samples with different ratio. The H_2 production by standard TiO_2 (P25) and boehmite nanoparticles are also reported for comparison. (b) Schematic illustration of the proposed H_2 production mechanism, pointing out the general steps involving electron/hole charge separation/reaction pathways. (c) Transient photocurrent response and (d) normalized open-circuit voltage-decay curves of Ti/Ge samples.

The mechanism of H_2 generation is expected to follow a similar pathway than that reported for TiO_2,[55,56] in the presence of methanol as sacrificial electron donor (SED). Instead of using a metal co-catalyst as a reduction site and electron collector, the natural polarization of Ti-doped nanotubes facilitates the photogenerated charge separation, making the reduction and oxidation sites spatially separated, as illustrated in **Figure 6b**. Details of the reaction are given in Supporting Information. In brief, the photogenerated charges (e^-/h^+) induce

dissociative adsorption of SED and hole scavenging, which is followed by hydrogen ion (H^+) release in the intern cavity of the nanotube. The reduction leading to the formation of a H_2 molecule is expected to be localized in the outer surface of the nanotubes, while the oxidation takes a place into the nanotubes (**Figure 6b**). This is probably a simplified view since the photo-reduction event depends on several parameters such as photo-generated charge-carrier recombination, vibronic coupling between donors (Ti/Ge sample) and acceptors (H_2O), accessibility of reactants to cite a few. However, at a first approximation, the smaller the energy gap between the donor (CB) and the acceptor (H_2O-redox potential), the faster the electron-transfer kinetics.[57] Our results show a correlation between the vicinity of the CB edge and the measured H_2 production. The difference between the CB edge and H_2O reduction redox potential is minimized for x = 0.2, 0.4 while these two samples display the highest photocatalytic activity.

Finally, the beneficial effect of natural polarization in photogenerated charge carrier is evaluated by assessing the transient photocurrent (PC) density and the charge transfer kinetic for each sample (**Figure 6c,d**). Pristine Ge-DWINTs exhibit the lowest current density, similar to the fluorine doped tin oxide (FTO) electrode, indicating low mobility of photogenerated charge generation as the optical band gap is higher (**Figure 6c**). Ti-doping of Ge-DWINTs results in an increased PC response. The intensity of the photocurrent during the ON/OFF light illumination cycles increases with Ti/Ge samples, reaching an optimal value for x = 0.4. Further increase in Ti-doping leads to a drastic drop of the photocurrent density, which translates the loss of the tubular structure and thus of the polarization properties. Among all the samples tested, Ti/Ge sample with x = 0.4 catalyst shows the highest PC density, in agreement with optimal photocatalytic H_2 evolution. In addition, we investigate the charge transfer kinetics in different Ti-doped Ge-DWINT photocatalysts by open-circuit voltage-decay (OCV) response. The normalized OCV curves obtained by relaxation upon interruption of the illumination for various samples are shown in **Figure 6d**. The greater amplitude observed for OCV between dark and illumination endows the photocatalyst larger photovoltage, indicating an efficient charge transport property. Interestingly, when monitoring the rate of OCV decay after turning off the light, the derived average charge carrier lifetime undergoes a significantly slower OCV decay process for Ti-doped samples. The lowest recovering decay was observed for 0.4. The OCV does not recover to the original level even after 700s based on the normalized OCV decay curves (**Figure 6d**). The transient decay profiles were fitted with a first-order kinetic model to obtain the pseudo-first-order recombination rate constant (k_r), such as:[58]

$$\frac{E - E_{\mathrm{ph}}}{E_0 - E_{\mathrm{ph}}} = 1 - \exp\left(-k_{\mathrm{r}} t\right)$$

where E is the open-circuit voltage decay at any time t while E_0 and E_{pH} represent the dark stationary OCV value and the photo-stationary OCV value, respectively. The k_{r} values for all photocatalysts are presented in **Table S2**, showing the lowest decay value for the most active Ti/Ge composite. We observe that the recombination rate constant k_{r} for the Ti/Ge DWINTs (x = 0.4) photocatalyst (1.42 10^{-3} s^{-1}) is 5 times smaller than pristine Ge-DWINT (7.01 10^{-3} s^{-1}), indicating that holes are more likely to perform water oxidation. In the meantime, the electrons accumulated in the Ti-doping Ge-DWINT (x = 0.4) photocatalyst have a longer lifetime.[58] The results confirm the effective charge carrier transport and separation when the Ti-doping operates while maintaining the imogolite tubular nanostructure. The presence of Ti atoms, even at a very low amount into the structure, modifies the electronic properties of imogolite nanotubes taking advantage of the natural polarization of the nanotubes, making them a promising photoactive tubular nanostructure.

3. Conclusion

We investigate the potential of synthetic double-walled imogolite nanotubes for photocatalytic applications. Substitution of Ge precursor by Ti precursors is carried out to transform pristine imogolite from non-photoactive material to a photocatalyst efficient for H_2 generation. Various Ti/Ge samples are prepared by changing the initial precursor ratio. The optimal condition is found around x = 0.4 for which the double-wall shape of the nanotube is preserved. The incorporation of Ti in a very small quantity in the nanotubes modifies its band structure sufficiently to confer them unique photocatalytic properties. The photocatalytic efficiency reveals a high hydrogen production of ~1500 µmol g^{-1} for noble metal-free photocatalyst, 65-fold higher than the commercial TiO_2P25. This enhanced H_2 production is attributed to different physico-chemical phenomena, such as preservation of the tubular structure, introduction of Ti atoms within the DWINT structure. This study represents a cornerstone for using modified imogolite nanotubes as novel photoactive nanoplatform and provide the first step toward exploiting the polarization properties of INTs to surpass existent photon conversion efficiencies from conventional materials in energetic and environmental photocatalytic reactions.

4. Experimental Section

Chemicals: Aluminum perchlorate nonahydrate, ($Al(ClO_4)_3$.9H2O, Reagent grade, Alfa Aesar), germanium (IV) ethoxide ($Ge(OC_2H_5)_4$, ≥99.95% trace metals basis, Sigma Aldrich), titanium (IV) isopropoxide ($C_{12}H_{28}O_4Ti$, 98+%, ACROS Organics™), Urea ($CO(NH_2)_2$, ACS reagent, >99.0%, Sigma Aldrich), and potassium bromide (KBr, IR grade, Merck) were used as received.

Synthesis of Ti/Ge samples: Germanium (IV) ethoxide and titanium (IV) isopropoxide are mixed at different ratios (x = [Ti]/([Ge]+[Ti]) = 0, 0.2, 0.4, 0.6, 0,8 and 1) under stirring in presence of an aluminum perchlorate solution with an [Al]/([Ge]+[Ti]) ratio equal to 2. [Ti] is the molar concentration of titanium isopropoxide and [Ge] that of germanium (IV) ethoxide. The initial aluminum perchlorate concentration is C = 0.2 $mol.L^{-1}$. We demonstrated previously that aluminum perchlorate is well-suited to obtain high yield of nanotubes and that perchlorates do not alter their morphology.[34] Within the same solution, an aqueous solution of urea at concentration of 0.2 $mol.L^{-1}$ is added as a source of hydroxyl ions during the thermal decomposition of $CO(NH_2)_2$. Solutions are stirred for 1h at room temperature in PFTE beakers. These beakers are placed in autoclaves (Parr Instrument) for hydrothermal treatment under autogenous pressure into an oven at 140 °C for 5 days. After the suspensions are cooled down, all samples are dialyzed against ultrapure water, using 10 kD membranes (Spectra/Por) to remove residuals salts and alcohol in excess until the conductivity is below 5 $\mu S.cm^{-1}$.

Electron microscopy: Conventional transmission electron microscopy (TEM observations on individual nanotubes were performed on a JEOL1400 microscope operating at 80 kV to avoid any electron beam damage. Dilute aliquot of Ti/Ge samples were prepared at 1 $mg.L^{-1}$ in ethanol. A drop of this mixture was deposited on a copper grid coated with carbon layer and dried at room temperature. The morphological parameters were measured over 200 individual particles. For cryo-TEM acquisition, a 4 µL of sample solution was deposited onto a holey carbon grid (Quantifoil R2/2) ionized by glow discharge and vitrified into liquid ethane cooled by liquid nitrogen using a Vitrobot Mark IV (Thermo Fisher Scientific) operated at 22 °C and 100% relative humidity. The grids were stored in liquid nitrogen until use. Frozen samples were transferred to a Gatan 626 cryo-holder (Gatan Inc.) and examined at -180°C in a JEOL JEM-2010F at 200 kV. The samples were imaged with a magnification of ×200,000 and were collected with a Gatan Ultrascan 4K CCD camera at 200 nm of nominal defocus under low-electron-dose conditions (9 $e^-.Å^{-2}$).

Scanning transmission electron microscopy (STEM) and X-ray energy dispersive spectroscopy (XEDS) measurements were conducted using the Argonne PicoProbe Analytical

Electron Microscope (AEM)[59] and the Thermo Fisher Scientific Titan Low-Base probe-corrected microscope. The AEM works presented here were conducted at 60 kV using also high-angle annular dark field (HAADF)-STEM imaging. Temporally resolved hyperspectral XEDS was carried out using the ANL XPAD system employing its ultra-sensitivity 4.5 sR detector. During imaging and hyperspectral measurements, the electron beam current on the specimen was < 100 pA.

Fourier-transform infrared spectroscopy (FTIR): FTIR spectra were recorded on dry sample powders using a Nicolet iS50 (Thermo Scientific) spectrometer equipped with a KBr beam splitter and a DTGS/KBr detector. The transmission measurements in the range 4000−400 cm^{-1} were performed by averaging 200 scans at a resolution of 4 cm^{-1}. Transparent pressed pellets were prepared by mixing about 1.5 mg of dry powder sample with 150 mg of transparent KBr, to guarantee 1 wt. % of sample inside the final pellet.

Wide-Angle X-ray scattering (WAXS): Prior to measurements, the samples were inserted into borosilicate capillary tubes of 1 mm diameter (GLAS, Schönwalde bei Berlin, Germany) and flame-sealed. WAXS experiments were carried out at the MORPHEUS platform (Laboratoire de Physique des Solides) by using rotating anode generators equipped with multilayer W/Si optics (Osmic). The measurements were performed at two different wavelengths λ ($\lambda_{CuK\alpha}$ = 0.1542 nm and $\lambda_{Mo\ K\alpha}$ = 0.0711 nm). Two-dimensional (2D) patterns were collected on a MAR345 detector (marXperts GmgH, Germany) with 150 µm pixel size. The sample-to-detector distance was set at 300 mm (Cu wavelength) and 150 mm (Mo wavelength). This configuration allows covering a wide range of scattering vector modulus Q = 1-50 nm^{-1} ($Q = 4\pi/\lambda \sin(\theta)$ with 2θ the scattering angle). The scattered intensity I as a function of Q is obtained from the angular integration of the scattering patterns.

X-ray Absorption Near Edge Structure (XANES): Al and Ti K-edges XANES experiments were undertaken at LUCIA beamline (Soleil synchrotron, France).[60] The X-ray beam was monochromated using either a pair of KTP (011) crystals (Al K-edge) or Si (111) crystal (Ti K-edge). Spectra were acquired with steps of 0.2 eV in the edge region and of 1 eV behind the edge, at a counting rate of 2 s per step. Data were recorded in fluorescence mode using a mono-element (60 mm^2) silicon drift diode detector and they were corrected for the detector dead time. Data processing, normalization and analysis of XANES spectra were performed using the Athena software.[61]

X-ray photoelectron spectroscopy (XPS): XPS analysis was performed using a Kratos Axis SUPRA XPS fitted with a monochromated Al Kα X-ray source (1486.7 eV), a spherical sector analyzer and 3 multichannel resistive plates, 128 channel delay line detectors. All data

was recorded at 150W and a spot size of 700 x 300 µm. Survey scans were recorded at a pass energy of 160 eV, and high-resolution scans were recorded at a pass energy of 20 eV. Electronic charge neutralization was achieved using a magnetic immersion lens. Filament current = 0.27 A, charge balance = 3.3 V, filament bias = 3.8 V. All data were recorded at a pressure below 10^{-8} Torr and at room temperature (294 K). Data was analyzed using CasaXPS (v2.3.19PR1.0). The energy shift due to electrostatic charging was subtracted using the carbon adventitious signal, i.e., the C 1s peak located at 284.8 eV. Peaks were fit with a Shirley background prior to component analysis with the appropriate experimental sensitivity factors of the normalized photo ionization cross-section of the atomic subshells as determined by Scofield.[62]

UV-vis spectroscopy: Optical properties of Ti/Ge samples were determined using UV-vis spectroscopy (model Cary 5000 series, Agilent Technologies) equipped with an integrating sphere for diffuse reflection measurements. The maximum reflectance was set to 100% using $BaSO_4$ as a reference in a wavelength range between 200 to 800 nm.

Hydrogen generation: The production of H_2 from an aqueous methanol solution was carried out following a procedure reported previously.[63] Experiments were performed in a closed quartz reactor and the reaction medium was previously purged with nitrogen gas (30 min) to remove O_2. The UV-visible light is delivered by a Xenon lamp (Oriel, 300 W) whose spectrum is reported in Figure S10. For these experiments, 20 mg of tested substance was suspended under vigorous stirring in 20 mL of a degassed aqueous solution (H_2O:MeOH, 3:1 v/v) used as a sacrificial agent. The produced H_2 was quantified by gas chromatography (GC, Agilent Technologies 7820A) using a thermal conductivity detector set at 250°C and nitrogen as carrier gas (flux: 22.5 mL min^{-1}, column of molecular sieve 5 Å and oven temperature at 50 °C). To assess the morphological stability, Ti/Ge samples with x = 0.2 and 0.4 were recovered after 5 hours of hydrogen generation. After drying, the recycled samples were analyzed by WAXS experiments. The related WAXS patterns (Figure S11) present the same characteristics as original samples with the oscillations representative of the double-walled nanotube form factor as well as the asymmetrical peak related to the axial periodicity along the nanotube axis. Therefore, the structural analysis of the two samples demonstrated that no changes has been observed, attesting of the stability of the Ti/Ge samples.

Photoelectrochemical studies: The electrochemical measurements were conducted in a three electrode rectangular quartz cell that consists of the as-prepared FTO (1 cm^2) electrode as the working electrode, Pt wire as a counter electrode, Ag/ AgCl as the reference electrode, and an aqueous Na_2SO_4 solution (0.5 M, without pH adjustment). The working electrode was

prepared as follows. 10 mg of the as-prepared Ti/Ge sample was dispersed in 5 ml of 2–propanol, and the suspension was dropcasted on a 1 cm^2 FTO glass plate. Finally, the obtained working electrodes were dried at room temperature overnight. The cell was illuminated by a Xe lamp irradiation using an AM 1.5 solar simulator.

Supporting Information

Supporting Information is available from the Wiley Online Library or from the author.

Acknowledgements

The authors acknowledge the financial support of the French ANR agency (ANR) under grand agreement ANR-18-CE09-0001 (C3PO) and CNRS through the International Emerging Actions program (no. 08216). This work is supported by a public grant from the "Laboratoire d'Excellence Physics Atoms Light Mater" (LabEx PALM) overseen by the French National Research Agency (ANR) as part of the "Investissements d'Avenir" program (reference: ANR-10-LABX-0039-PALM) and by the Region Ile-de-France in the framework of DIM Respore. P.J.-C. received funding from the European Union's Horizon Europe research and innovation program under the Marie Skłodowska-Curie grant agreement No: 101068996. The results used the Imagerie- Gif core facility supported by l'Agence Nationale de la Recherche (ANR-11-EQPX-0029/Morphoscope, ANR-10-INBS-04/FranceBioImaging; ANR- 11- IDEX- 0003- 02/ Saclay Plant Sciences). Cryo-TEM experiments were supported by the METSA network (Proposal FR3507) and by the French Investissements d'Avenir LabEx PALM (ANR-10LABX-0039PALM). This project has received funding from the European Union's Horizon 2020 research and innovation programme under grant agreement No 823717 – ESTEEM3 (SIMSINE project). RA acknowledges funding by the Spanish MCIN (PID2019-104739GB-100/AEI/10.13039/501100011033). The work at Argonne National Laboratory was supported by the U.S. Department of Energy, Office of Science, Office of Basic Energy Sciences, under Contract No. DE-AC02-06CH11357. The X-ray photoelectron (XPS) data collection was performed at the EPSRC National Facility for XPS ("HarwellXPS"), operated by Cardiff University and UCL, under Contract No. PR16195. The authors thank Emmanuel Joussein and Alexandra Courtin for access to LUCIA experiments (SOLEIL, proposal 20180745). Many fruitful discussions with G. Teobaldi are gratefully acknowledged.

Received: ((will be filled in by the editorial staff))

Revised: ((will be filled in by the editorial staff))

Published online: ((will be filled in by the editorial staff))

References

[1] B. Weng, S. Liu, Z.-R. Tang, Y.-J. Xu, *Rsc Adv.* **2014**, *4*, 12685.
[2] S. Liu, Z.-R. Tang, Y. Sun, J. C. Colmenares, Y.-J. Xu, *Chem. Soc. Rev.* **2015**, *44*, 5053.
[3] M. Xiao, Z. Wang, M. Lyu, B. Luo, S. Wang, G. Liu, H.-M. Cheng, L. Wang, *Adv. Mater.* **2019**, *31*, 1801369.
[4] J. Kou, C. Lu, J. Wang, Y. Chen, Z. Xu, R. S. Varma, *Chem. Rev.* **2017**, *117*, 1445.
[5] K. Woan, G. Pyrgiotakis, W. Sigmund, *Adv. Mater.* **2009**, *21*, 2233.
[6] F. He, G. Chen, J. Miao, Z. Wang, D. Su, S. Liu, W. Cai, L. Zhang, S. Hao, B. Liu, *ACS Energy Lett.* **2016**, *1*, 969.
[7] M. Ge, Q. Li, C. Cao, J. Huang, S. Li, S. Zhang, Z. Chen, K. Zhang, S. S. Al- Deyab, Y. Lai, *Adv. Sci.* **2017**, *4*, 1600152.
[8] J. L. Blackburn, *ACS Energy Lett.* **2017**, *2*, 1598.
[9] D. Jiang, H. Jing, Z. Liu, C. Jia, Q. Liu, *J. Phys. Chem. C* **2021**, *125*, 15316.
[10] S. Linic, P. Christopher, D. B. Ingram, *Nat. Mater.* **2011**, *10*, 911.
[11] A. G. Dosado, W.-T. Chen, A. Chan, D. Sun-Waterhouse, G. I. Waterhouse, *J. Catal.* **2015**, *330*, 238.
[12] M. Wang, M. Ye, J. Iocozzia, C. Lin, Z. Lin, *Adv. Sci.* **2016**, *3*, 1600024.
[13] P. Jiménez-Calvo, V. Caps, V. Keller, *Renew. Sustain. Energy Rev.* **2021**, 111095.
[14] F. Chen, H. Huang, L. Guo, Y. Zhang, T. Ma, *Angew. Chem. Int. Ed.* **2019**, *58*, 10061.
[15] E. Paineau, *Appl. Sci.* **2018**, *8*, 1921.
[16] E. Paineau, P. Launois, in *Nanomater. Clay Miner.*, Elsevier, **2019**, pp. 257–284.
[17] J. Govan, N. Arancibia-Miranda, M. Escudey, B. Bonelli, F. Tasca, *Mater. Chem. Front.* **2021**, *5*, 6779.
[18] E. Poli, J. D. Elliott, L. E. Ratcliff, L. Andrinopoulos, J. Dziedzic, N. D. M. Hine, A. A. Mostofi, C.-K. Skylaris, P. D. Haynes, G. Teobaldi, *J. Phys.-Condens. Matter* **2016**, *28*, 074003.
[19] J. D. Elliott, E. Poli, I. Scivetti, L. E. Ratcliff, L. Andrinopoulos, J. Dziedzic, N. D. M. Hine, A. A. Mostofi, C.-K. Skylaris, P. D. Haynes, G. Teobaldi, *Adv. Sci.* **2017**, *4*, 1600153.
[20] G. Monet, M. S. Amara, S. Rouzière, E. Paineau, Z. Chai, J. D. Elliott, E. Poli, L.-M. Liu, G. Teobaldi, P. Launois, *Nat. Commun.* **2018**, *9*, 2033.
[21] A. Kudo, Y. Miseki, *Chem. Soc. Rev.* **2009**, *38*, 253.
[22] J. Li, P. Jiménez-Calvo, E. Paineau, M. N. Ghazzal, *Catalysts* **2020**, *10*, 89.
[23] M.-C. Pignié, S. Patra, L. Huart, A. R. Milosavljević, J. P. Renault, J. Leroy, C. Nicolas, O. Sublemontier, S. Le Caër, A. Thill, *Nanoscale* **2021**, *13*, 19650.
[24] L. Guimaraes, A. N. Enyashin, J. Frenzel, T. Heine, H. A. Duarte, G. Seifert, *Acs Nano* **2007**, *1*, 362.
[25] M. P. Lourenco, L. Guimaraes, M. C. da Silva, C. de Oliveira, T. Heine, H. A. Duarte, *J. Phys. Chem. C* **2014**, *118*, 5945.
[26] E. Shafia, S. Esposito, M. Armandi, E. Bahadori, E. Garrone, B. Bonelli, *Catal. Today* **2016**, *277*, 89.
[27] E. Bahadori, V. Vaiano, S. Esposito, M. Armandi, D. Sannino, B. Bonelli, *Catal. Today* **2018**, *304*, 199.
[28] F. Alvarez-Ramirez, *J. Chem. Theory Comput.* **2009**, *5*, 3224.

[29] I. S. Popov, A. N. Enyashin, *Phys. Status Solidi B* **2021**, *258*, 2100188.
[30] M.-S. Amara, E. Paineau, M. Bacia-Verloop, M.-E. M. Krapf, P. Davidson, L. Belloni, C. Levard, J. Rose, P. Launois, A. Thill, *Chem. Commun.* **2013**, *49*, 11284.
[31] P. de S. Santos, A. C. V. Coelho, H. de S. Santos, P. K. Kiyohara, *Mater. Res.* **2009**, *12*, 437.
[32] T. Tachikawa, M. Fujitsuka, T. Majima, *J. Phys. Chem. C* **2007**, *111*, 5259.
[33] Y.-Y. Liao, P. Picot, J.-B. Brubach, P. Roy, A. Thill, S. Le Caer, *J. Phys. Chem. C* **2019**, *123*, 19768.
[34] E. Paineau, S. Rouzière, G. Monet, C. C. Diogo, I. Morfin, P. Launois, *J. Colloid Interface Sci.* **2020**, *580*, 275.
[35] S. Wada, K. Wada, *Clays Clay Miner.* **1982**, *30*, 123.
[36] I. Bottero, B. Bonelli, S. E. Ashbrook, P. A. Wright, W. Zhou, M. Tagliabue, M. Armandi, E. Garrone, *Phys. Chem. Chem. Phys.* **2011**, *13*, 744.
[37] A. Boumaza, L. Favaro, J. Lédion, G. Sattonnay, J. B. Brubach, P. Berthet, A. M. Huntz, P. Roy, R. Tétot, *J. Solid State Chem.* **2009**, *182*, 1171.
[38] J. Cambedouzou, M. Chorro, R. Almairac, L. Noé, E. Flahaut, S. Rols, M. Monthioux, P. Launois, *Phys. Rev. B* **2009**, *79*, 195423.
[39] P. Maillet, C. Levard, E. Larquet, C. Mariet, O. Spalla, N. Menguy, A. Masion, E. Doelsch, J. Rose, A. Thill, *J. Am. Chem. Soc.* **2010**, *132*, 1208.
[40] E. Paineau, M.-E. M. Krapf, M.-S. Amara, N. V. Matskova, I. Dozov, S. Rouzière, A. Thill, P. Launois, P. Davidson, *Nat. Commun.* **2016**, *7*, 10271.
[41] S. Goriparti, U. Gulzar, E. Miele, F. Palazon, A. Scarpellini, S. Marras, S. Monaco, R. Proietti Zaccaria, C. Capiglia, *J. Mater. Chem. A* **2017**, *5*, 19721.
[42] P. Harshavardhan Reddy, A. V. Kir'yanov, A. Dhar, S. Das, D. Dutta, M. Pal, Y. O. Barmenkov, J. A. Minguella-Gallardo, S. K. Bhadra, M. C. Paul, *Appl. Opt.* **2017**, *56*, 9315.
[43] K. Prabhakaran, T. Ogino, *Surf. Sci.* **1995**, *325*, 263.
[44] W. Wang, D. Lei, Y. Dong, X. Gong, E. S. Tok, Y. C. Yeo, *Sci. Rep.* **2017**, *7*, DOI 10.1038/s41598-017-01449-1.
[45] S. Mukherjee, V. M. Bartlow, S. Nair, *Chem. Mater.* **2005**, *17*, 4900.
[46] S. Swaminathan, Y. Sun, P. Pianetta, P. C. McIntyre, *J. Appl. Phys.* **2011**, *110*, 094105.
[47] K. Kim, H. Choi, J. H. Kim, *Appl. Surf. Sci.* **2017**, *416*, 527.
[48] P. Jiménez-Calvo, V. Caps, M. N. Ghazzal, C. Colbeau-Justin, V. Keller, *Nano Energy* **2020**, 104888.
[49] M. N. Ghazzal, N. Chaoui, M. Genet, E. M. Gaigneaux, D. Robert, *Thin Solid Films* **2011**, *520*, 1147.
[50] J. T. Kloprogge, L. V. Duong, B. J. Wood, R. L. Frost, *J. Colloid Interface Sci.* **2006**, *296*, 572.
[51] G. Monet, S. Rouzière, D. Vantelon, C. Coelho Diogo, D. Maurin, J.-L. Bantignies, P. Launois, E. Paineau, *J. Phys. Chem. C* **2021**, *125*, 12414.
[52] P. Ildefonse, D. Cabaret, P. Sainctavit, G. Calas, A.-M. Flank, P. Lagarde, *Phys. Chem. Miner.* **1998**, *25*, 112.
[53] F. Farges, G. E. Brown, J. J. Rehr, *Phys. Rev. B* **1997**, *56*, 1809.
[54] C. Wang, J. Li, E. Paineau, A. Laachachi, C. Colbeau-Justin, H. Remita, M. N. Ghazzal, *J. Mater. Chem. A* **2020**, DOI 10.1039/c9ta12665a.
[55] T. Kawai, T. Sakata, *J. Chem. Soc. Chem. Commun.* **1980**, 694.
[56] G. D. Gesesse, C. Wang, B. K. Chang, S.-H. Tai, P. Beaunier, R. Wojcieszak, H. Remita, C. Colbeau-Justin, M. N. Ghazzal, *Nanoscale* **2020**, *12*, 7011.
[57] A. Nitzan, *Chemical Dynamics in Condensed Phases: Relaxation, Transfer and Reactions in Condensed Molecular Systems*, Oxford University Press, **2006**.
[58] H. Kim, D. Monllor-Satoca, W. Kim, W. Choi, *Energy Environ. Sci.* **2015**, *8*, 247.

[59] N. Zaluzec, *Microsc. Microanal.* **2021**, *27*, 2070.
[60] D. Vantelon, N. Trcera, D. Roy, T. Moreno, D. Mailly, S. Guilet, E. Metchalkov, F. Delmotte, B. Lassalle, P. Lagarde, *J. Synchrotron Radiat.* **2016**, *23*, 635.
[61] B. Ravel, M. Newville, *J. Synchrotron Radiat.* **2005**, *12*, 537.
[62] J. H. Scofield, *J. Electron Spectrosc. Relat. Phenom.* **1976**, *8*, 129.
[63] G. D. Gesesse, C. Li, E. Paineau, Y. Habibi, H. Remita, C. Colbeau-Justin, M. N. Ghazzal, *Chem. Mater.* **2019**, *31*, 4851.